Controllable conical magnetic structure and spin-orbit-torque switching in symmetry-broken ferrimagnetic films

Yaqin Guo,[1,†] Jing Zhang,[1,†] Purnima P. Balakrishnan,[2] Alexander J. Grutter,[2] Baishun Yang,[3] Michael R. Fitzsimmons,[4,5,6] Timothy R. Charlton,[5] Haile Ambaye,[5] Xu Zhang,[1] Hanshen Huang,[7] Zhi Huang,[1] Jinyan Chen,[1] Chenyang Guo,[3] Xiufeng Han,[3] Kang L. Wang,[7] and Hao Wu[1,3,7,*]

[1] *Songshan Lake Materials Laboratory, Dongguan, Guangdong 523808, China*
[2] *NIST Center for Neutron Research, National Institute of Standards and Technology, Gaithersburg, Maryland 200899, USA*
[3] *Beijing National Laboratory for Condensed Matter Physics, Institute of Physics, Chinese Academy of Sciences, Beijing 100190, China*
[4] *Neutron Scattering Division, Oak Ridge National Laboratory, Oak Ridge, Tennessee 37831, USA*
[5] *Department of Physics and Astronomy, University of Tennessee, Knoxville, Tennessee 37996, USA*
[6] *Shull Wollan Center – A Joint Center for Neutron Sciences, Oak Ridge, Tennessee 37831, USA*
[7] *Department of Electrical Engineering, University of California, Los Angeles, California 90095, USA*

(Received 27 February 2023; revised 28 September 2023; accepted 5 January 2024; published 23 January 2024; corrected 7 February 2024)

Exploring and controlling chiral spin textures has attracted enormous interest from the perspective of fundamental research and spintronic applications. Here, we report the emergence of spiral spin states, bulk spin-orbit torque (SOT), and the Dzyaloshinskii-Moriya interaction (DMI) induced with the combination of Bloch- and Néel-type in a single Gd-Fe-Co layer with a vertical composition gradient. Using polarized neutron reflectometry, the magnetization $\mathbf{M}$ is found to rotate with depth through the gradient, due to the nonzero out-of-plane DMI ($\mathbf{D}_{\mathrm{OOP}}$). Meanwhile, the deterministic SOT magnetization switching in a single Gd-Fe-Co layer without a heavy metal, where the sign of the bulk SOT and in-plane DMI ($\mathbf{D}_{\mathrm{IP}}$) is governed by the direction of the composition gradient. The presented results pave the way for flexibly engineering the spin currents and DMI in the ferrimagnetic materials, which have potential applications for future ferrimagnetic SOT devices.

DOI: 10.1103/PhysRevApplied.21.014045

I. INTRODUCTION

Symmetry may be described as the presence of physical characteristics of a system, which are invariant under certain transformations. The presence of spatial symmetry in materials systems is necessary for the realization of many physical phenomena, including topological insulators [1], quantum entanglement [2,3], and superconductivity [4,5]. However, other physical phenomena require specific forms of asymmetry to emerge, as in the case of time-reversal symmetry breaking in topological insulators leading to the quantum anomalous Hall effect. Alternatively, broken inversion symmetry induces the Dzyaloshinskii-Moriya interaction (DMI) [6,7], which has implications in magnetic systems for its tendency to favor spin configurations, which rotate around a local characteristic vector $\mathbf{D}$. This can destabilize the uniformly magnetized states and lead to alternative chiral magnetic orders, such as magnetic skyrmions [8–10] and chiral domain walls [11–14], which result in fascinating physical behaviors [15–17] with the potential for application in future spintronic devices [9,18].

One key application of broken symmetry in alternative devices is the application of nonequilibrium transport phenomena, such as current-induced spin-orbit torques (SOTs) to efficiently control spin orientation through angular momentum transfer. Such SOT switching has been widely investigated in both multilayer heterostructures and bulk noncentrosymmetric conductors and semiconductors [19]. The prototypical implementation of a SOT multilayer heterostructure is a heavy metal/ferromagnet (HM/FM) bilayer in which the SOT can arise from either the spin Hall effect (SHE) in the HM [20–22], the Rashba effect at the interface [23–25], or both. Regardless of the origin, the induced SOT in a HM/FM bilayer is interfacial, so that only a relatively thin FM layer can be switched. Such thickness limitations come with challenges in achieving high thermal stability. An alternative candidate system

---

[*] wuhao1@sslab.org.cn
[†] These authors contributed equally to this work.

is the family of bulk noncentrosymmetric conductors and semiconductors, which includes single-layer crystals with bulk inversion asymmetry, such as Cu-Mn-As or (Ge, Mn)Te [26], and materials with locally broken inversion symmetry, such as Mn_2Au [27]. These materials lacking inversion symmetry have great promise for SOT-induced magnetization switching in thicker, more bulklike layers. Ferrimagnetic SOT heterostructures have attracted particular attention in recent years thanks to the competition between multiple magnetic sublattices, which enables unconventional spin dynamics and allows the net magnetization to be tuned separately from the transport properties. By tuning the system to be near the magnetization compensation temperature T_M or the angular momentum compensation temperature T_A, a highly efficient spin-orbit torque or spin-transfer torque can be generated [28–30]. Furthermore, the disappearance of the skyrmion Hall effect, which is expected in antiferromagnets, has also been reported at T_A for ferrimagnets [31,32]. Since they are antiferromagnetically coupled, their topological charges are opposite. Each of these make ferrimagnets even more promising candidates for spintronic applications. It has recently been reported that rare earth (RE) transition metal (TM) ferrimagnetic (FMI) alloys with inversion asymmetry along the growth direction can exhibit deterministic spin-orbit torque switching and noncollinear DMI [33,34]. In Gd-Fe-Co ferrimagnetic alloys, strong spin-orbit interactions are expected from the 5*d* band of Gd, and the presence of large SOC effects has been demonstrated by the well-defined Rashba surfaces found in Gd metal [35,36]. The existence of such Rashba surface states is a common characteristic of rare-earth metals and metallic compounds possessing a conduction band with 5*d* states [35,37,38], which give rise to desirable magnetic properties. Given that the magnetic properties of bilayers can be dependent on the stacking sequence, it is crucial to study and optimize the magnetism and the electrical transport in a single Gd-Fe-Co layer.

Here, we report the emergence of spiral spin states, the deterministic SOT-induced magnetization switching, and the DMI induced with the combination of Bloch- and Néel-type in a single Gd-Fe-Co layer with a vertical composition gradient. PNR measurements demonstrate the rotation of magnetization **M** in depth through the compositional gradient, suggesting a nonzero Bloch-type $\mathbf{D}_{OOP}$. We also demonstrate deterministic SOT magnetization switching in a single Gd-Fe-Co layer without a heavy metal, where the sign of the bulk SOT and Néel-type $\mathbf{D}_{IP}$ is governed by the direction of the composition gradient. Thus, both Bloch- and Néel-type result from the intentional inversion asymmetry in the *z* direction in these Gd-Fe-Co single-layer samples. This may advance the practical applications exploiting the rich physics mechanism of spin-orbit effects in the FMI system.

II. RESULTS AND DISCUSSION

The MgO(2)/$Gd_x(FeCo)_{1-x}$(10)/MgO(2)/Ta(2) (thicknesses in nanometers) structured films with various Gd compositions (x) are grown on the Si/SiO_2 substrates by magnetron sputtering in a system maintained at a base pressure of 5×10^{-8} Torr. During the deposition, the Ar atmosphere is maintained with the pressure of 3 mTorr. The MgO layer was deposited by rf sputtering, and the metal layers were deposited by dc sputtering. The $Gd_x(FeCo)_{1-x}$ film is deposited by co-sputtering two off-axis targets Gd and CoFe positioned at opposite sides (along the y axis) at the same speed (0.34 Å/s) while rotating the Si/SiO_2 substrate. The composition of Gd-CoFe is tuned by changing the power of the CoFe source from 90 to 110 W (or 110 to 90 W), during which the power of Gd sources is kept constant (20 W), and the nominal composition is calibrated using the deposition rates of individual Gd and CoFe films. The ferrimagnet consists of ten sublayers of Gd-Fe-Co with different Gd compositions, where each sublayer is 1 nm thick. Figure 1(a) shows the bottom-layer composition as $Gd_{0.26}(FeCo)_{0.74}$ and the top-layer composition as $Gd_{0.14}(FeCo)_{0.86}$, and the internal nine deposited layers followed a certain Gd composition step $\delta = 0.013$. The composition can be expressed as $Gd_{0.26-n}(FeCo)_{0.74+n\delta}$, where $n = 1, 2, 3 \ldots 9$. Seed and cap layers of MgO were grown to eliminate the relative interfacial effect, meanwhile the MgO cap can minimize oxidation of this metal structure. The bottom of the sample is dominated by Gd, while the decrease of the Gd composition towards the top of the sample, and the top of the sample is dominated by CoFe. The decreasing composition gradient $\nabla Gd < 0$ leads to an evolution of the overall M_s of the sample. Here, the magnetic composition gradients x is from 0.26 to 0.14, in which the M_s approaches zero at $x = 0.26$, which correspond to the magnetic compensation point of $Gd_x(FeCo)_{1-x}$ at room temperature [39]. Note that the magnetic composition gradients of each layer (1 nm) here, with the bottom composition $Gd_{0.26}(FeCo)_{0.74}$ is close to the magnetic compensation point. Reversing the composition gradient $\nabla Gd > 0$, from the bottom layer with composition $Gd_{0.14}(FeCo)_{0.86}$ to the top layer with composition $Gd_{0.26}(FeCo)_{0.74}$ as shown in Fig. 1(d), results in the sample evolving from FeCo- to Gd-dominated magnetization. Scanning transmission electron microscopy high-angle annular dark-field (STEM HAADF) [Figs. 1(b) and 1(e)] and energy-dispersive x-ray spectroscopy (EDS) [Figs. 1(c) and 1(f)] were performed on the sample to verify the existence and quantify the composition gradient of the Gd-FeCo. The vertical lines (blue) in Figs. 1(b) and 1(e) represent the regions of EDS analysis. EDS curves versus the thickness direction in Figs. 1(c) and 1(f) exhibit a prominent linear gradient of Fe elements as designed. Both samples, with $\nabla Gd < 0$ and $\nabla Gd > 0$, show opposite

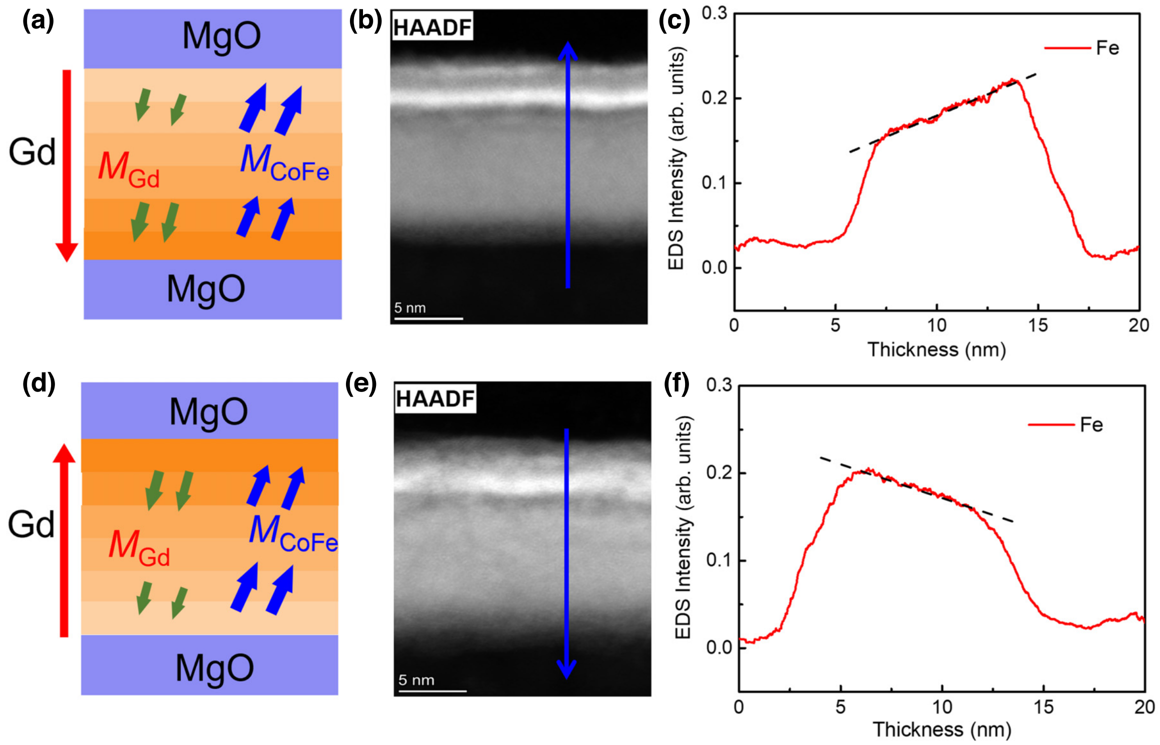

FIG. 1. Schematic depiction of composition gradient in the $Gd_x(FeCo)_{1-x}$ samples of the $\nabla Gd < 0$ (a)–(c) and $\nabla Gd > 0$ (d)–(f). High-resolution HAADF image of the $\nabla Gd < 0$ (b) and $\nabla Gd > 0$ (e). The corresponding EDS-measured Fe intensity in the samples (c),(f), as a function of vertical position marked with the blue line in (b),(e), respectively. Here, 0 nm is the surface of the film.

slopes, with an Fe-rich top or bottom, respectively, verifying the existence as well as the direction of the composition gradient.

In order to directly probe the magnetic and structural depth profile of the samples along the growth direction, polarized neutron reflectometry (PNR) experiments were carried out using the Magnetism Reflectometer (BL-4A) at the Spallation Neutron Source at Oak Ridge National Laboratory [40]. The Magnetism Reflectometer operates in time-of-flight mode, in which a collimated polychromatic beam of polarized neutrons with a wavelength band $\Delta\lambda = 0.45$ nm to 1.05 nm is incident on the film at a grazing incidence angle $\theta < 5°$. A magnetic field was applied along the incident beam path, primarily in plane. The neutrons interact in the film both with atomic nuclei and net magnetization. The reflected beam intensities measured at multiple angles θ were reduced using a Jupyter notebook approach [41,42] and fit simultaneously using a slab model in refl1d [43]. By polarizing the spin eigenstate of the incident neutron beam, parallel (↑) or antiparallel (↓) to the beam direction, and analyzing the reflected spin state, it is possible to separate the in-plane components of the magnetization. A magnetization perpendicular to the incident neutron spin polarization causes the neutron spin to flip during the scattering interaction. Thus, the non-spin-flip (NSF) neutron reflectivities ($R\uparrow\uparrow$ and $R\downarrow\downarrow$) are sensitive to the component of the magnetization along the axis of the neutron polarization, while the spin-flip (SF) neutron reflectivities ($R\uparrow\downarrow$ and $R\downarrow\uparrow$) probe the in-plane magnetization component perpendicular to the incident neutron polarization. By combining the results from NSF and SF neutron reflectivities, the magnitude and direction of the magnetization as a function of depth can be determined.

PNR measurements were performed on samples with both negative and positive gradients in magnetic fields ranging from 18 mT to 4.5 T; the results for these two samples are illustrated in Figs. 2 and S1 (see the Supplemental Material [44]), respectively. The NSF $R\uparrow\uparrow$ and $R\downarrow\downarrow$ cross sections [Fig. 2(a)] exhibit a peak with significant splitting at approximately $Q = 0.09$ nm^{-1} even up to large fields. To better visualize this feature, we plot the Fresnel-scaled difference between the two NSF cross sections at 250 mT and 4.5 T in Fig. 2(b), where defined as the $(R\uparrow\uparrow - R\downarrow\downarrow)/(R\uparrow\uparrow + R\downarrow\downarrow)$. It can clearly be seen that the fits are an excellent description of the data. And the obvious oscillation behavior of Fresnel-scaled difference was observed, indicating that the magnetic moment from in plane can be detected by PNR. Furthermore, the small splitting at low Q represents a small average magnetization along the field direction through the entire film, while large positive and negative splitting features at a high-Q point to a magnetic superstructure with a very well-defined

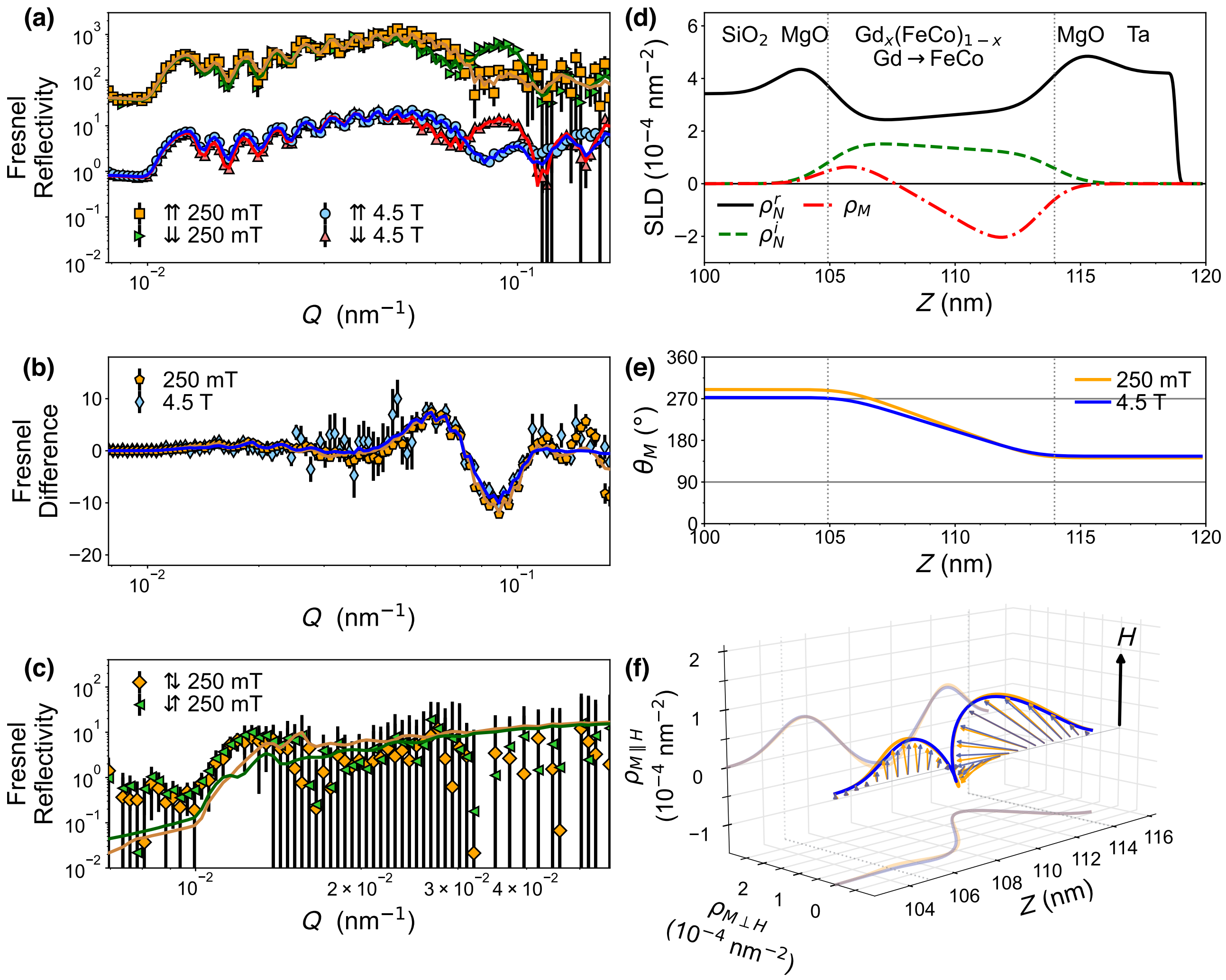

FIG. 2. (a) The NSF PNR reflectivities for the $\nabla\text{Gd} < 0$ sample in applied fields of 4.5 T and 250 mT (offset for clarity). (b) The corresponding difference between the NSF PNR reflectivities obtained from the experimental and calculated reflectivities. (c) The SF PNR reflectivities for the $\nabla\text{Gd} < 0$ sample in the field of 250 mT. (d) The nuclear SLD_N and magnetization SLD_M depth profiles of the sample, which best fit the PNR data. Here, $Z = 0$ nm corresponds to the Si substrate, which has approximately 100 nm of thermal oxide on top. (e) The angle of the magnetic moment with depth at the fields of 250 mT and 4.5 T, where $\theta = 270°$ corresponds to the direction of the applied field. (f) Vector plot of the magnetization.

periodicity smaller than the film thickness; similar PNR features are often associated with Bragg reflections in superlattices or spiral structures [45]. For the inverse gradient sample ($\nabla\text{Gd} > 0$) [Fig. S1(a) in the Supplemental Material [44]], the $R\uparrow\uparrow$ and $R\downarrow\downarrow$ curves are not coincident under the fields of 18 mT and 4.5 T. And a larger splitting is also shown at approximately $Q = 0.09\ \text{nm}^{-1}$ under 4.5 T compared to the field of 18 mT. Here, the value magnetic field of 18 mT is applied, which is less than the effective magnetic anisotropy. The oscillations peak under the field of 18 mT is more significant than that of 4.5 T from the Fresnel-scaled difference [Fig. S1(b) in the Supplemental Material [44]], indicating that the detected stronger magnetic moment along the magnetic field for $\nabla\text{Gd} > 0$ sample, compared to the $\nabla\text{Gd} < 0$ sample. [See the vertical projections (see the $\rho_\text{M} \parallel H$) in Figs. 2(f) and S1(f) in the Supplemental Material [44]].

Here, the magnetic structure of these graded Gd-Fe-Co layers is such that the only way to fit the NSF PNR datasets alone is through an oscillation in the magnetization component along the applied field direction at all measured fields [see the red and blue dotted lines in Figs. S2 and S3, or the $\rho_\text{M} \parallel H$ in Figs. 2(f) and S1(f) in the Supplemental Material [44]]. Such an oscillatory moment is unexpected, as the samples have been designed to exhibit a linearly varying magnetization with depth, passing through the compensation point near the middle of the Gd-Fe-Co. One way to reproduce this apparent oscillation in ρ_M is if the oscillation is the result of viewing the projection of a spiral along the neutron polarization direction while the magnetization varies linearly. Such a projection would produce the magnetic SLD curves shown in Figs. S2 and S3 in the Supplemental Material [44], and fits the NSF data extremely well, suggesting that there may be some form of spiral magnetic structure in the film. The zero crossings of this oscillating moment can be due to the film grading passing through the compensation point ($\rho_M = 0$) or by the rotation of the moment perpendicular to the applied field. A tight spiral with no compensation point present in the film could result in the same oscillation of the moment along the field, and would result in a similar oscillatory moment perpendicular to the field, which cancels out any net moment. The SF reflectivity is critical to resolving these ambiguities through sensitivity to the in-plane magnetization perpendicular to the applied field direction. As shown in Figs. 2(c) and S1(c) in the Supplemental Material [44], strong SF signals ($R\uparrow\downarrow$ and $R\downarrow\uparrow$) are observed near the critical edge at 250 and 18 mT and clearly suggest the presence of a net perpendicular magnetization in the PNR data. Together these suggest a periodic rotation of the moments within the film plane.

Quantitative modeling of the full polarization analysis PNR data confirms a spiral magnetic structure. The best-fit depth profiles of the complex nuclear-scattering length density ($\mathrm{SLD_N}$) and magnetic scattering length density ($\mathrm{SLD_M}$) are shown in Fig. 2(d). The nuclear reflection (ρ_N^r, real $\mathrm{SLD_N}$, black) shows clearly distinct layers of the heterostructure, and as designed, increases linearly as the Fe content increases. Of the elements present, Gd has a uniquely large neutron absorption cross section (ρ_N^i, imaginary $\mathrm{SLD_N}$, green) at these neutron energies [46]; the large absorption as represented by the green dashed line in Fig. 2(d) decreases linearly as the Gd content decreases, agreeing with the designed gradient $\nabla\mathrm{Gd} < 0$, but indicating a higher Gd concentration than 26%. Gd is the only element present with any significant neutron absorption cross section, which can contribute to the total imaginary SLD. The imaginary SLD of pure Gd metal in the 4–6 Angstrom range is $3.29 \times 10^{-4}\ \mathrm{nm^{-2}}$, so a $\mathrm{Gd_{0.26}(FeCo)_{0.74}}$ composition would have an imaginary SLD of $0.85 \times 10^{-4}\ \mathrm{nm^{-2}}$, which is significantly lower than the observed values in the range of $(1–2) \times 10^{-4}\ \mathrm{nm^{-2}}$. Although we can use a range of values of the absorption to fit the data, lowering the value to what is required for a 26% composition cannot describe the data. Though 26% Gd is supposed to be the compensation point, we see both that (1) these films pass through the compensation point and (2) all regions have significantly more than 26% Gd. Oxidation through the capping layers may reduce the Gd moment, shifting the compensation point.

Therefore, the magnetization cannot be described as a linearly varying magnetization along the applied field. Instead, we find that while the magnitude of the magnetization (ρ_M, magnetic SLD, red) [Fig. 2(d)] does linearly vary, passing through $\mathrm{SLD_M} = 0$ at the compensation point between the Gd-dominant bottom and FeCo-dominant top of the film, the in-plane angle (θ_M) [Fig. 2(e)] also linearly varies, resulting in an asymmetric helical structure as shown in Fig. 2(f). As the field is increased to 4.5 T, the moments rotate to have a larger component aligned with the field; however, the spiral persists even at these high fields. The same measurements are performed for the sample with opposite compositional gradient of $\nabla\mathrm{Gd} > 0$. As shown in Figs. S1(a)–S1(f) (see the Supplemental Material [44]), a similar helical magnetic structure is observed, consistent with that of $\nabla\mathrm{Gd} < 0$ sample. Both graded Gd-Fe-Co layers exhibit this helical structure rotating within the film plane; high fields of 4.5 T are not sufficient to align all moments along the field. This suggests that there is a nonzero component of DMI $\mathbf{D}_{\mathrm{OOP}}$ along the out-of-plane direction.

Having demonstrated the presence of a spiral structure and linear magnetization gradient through the compensation point, we now turn our attention to the electrical transport properties and characterize the current-induced magnetization switching. We patterned $\mathrm{MgO/Gd}_x\mathrm{(FeCo)}_{1-x}\mathrm{/MgO}$ films into the Hall bar device with a 20 μm width by a standard photolithography method combined with a dry-etching process. Cr(20 nm)/Au(100 nm) electrodes were fabricated for making contact to the Hall bar channel. The SOT-induced magnetization switching was measured by sweeping a writing current pulse J_e for 1 ms to switch state, waiting for 1 s, then applying a much smaller reading current pulse (1 mA) and measuring the Hall resistance R_{xy} to detect the magnetic moment out of plane. Figures 3(a) and 3(b) show the $R_{xy} - J_e$ loops for the $\nabla\mathrm{Gd} < 0$ sample at room temperature under in-plane magnetic field H_x of ±100 Oe, respectively, where H_x is applied to break the mirror symmetry for deterministic switching [21]. The critical switching current density J_c was found to be $1.3 \times 10^7\ \mathrm{A\ cm^{-2}}$. For the $\nabla\mathrm{Gd} > 0$ sample [Figs. 3(c) and 3(d)], the SOT switching polarity ($R_{xy} - J_e$) is reversed compared to the $\nabla\mathrm{Gd} < 0$ sample [Figs. 3(a) and 3(b)], but the J_c ($1.2 \times 10^7\ \mathrm{A\ cm^{-2}}$) is in excellent agreement with the value obtained from the $\nabla\mathrm{Gd} < 0$ sample. Both $R_{xy} - J_e$ loops of opposite gradient compositions have the opposite polarity, indicating that the vertical symmetry breaking of these two samples have opposite signs, confirming that the SOTs in the Gd-Fe-Co layer originate from the vertical composition gradient. For a more quantitative examination of the SOT-switching efficiency, we probed the effective spin-orbit fields.

Specifically, we quantified the SOT efficiency using standard harmonic Hall measurements [47,48]. An external in-plane magnetic field H_x is again applied for deterministic switching, and an additional small magnetic anisotropy field H_k is applied along the x axis. In this condition, we apply an ac current of the form $J_e = J_0 \sin\omega t$, along the x axis. The SOT-induced alternating effective

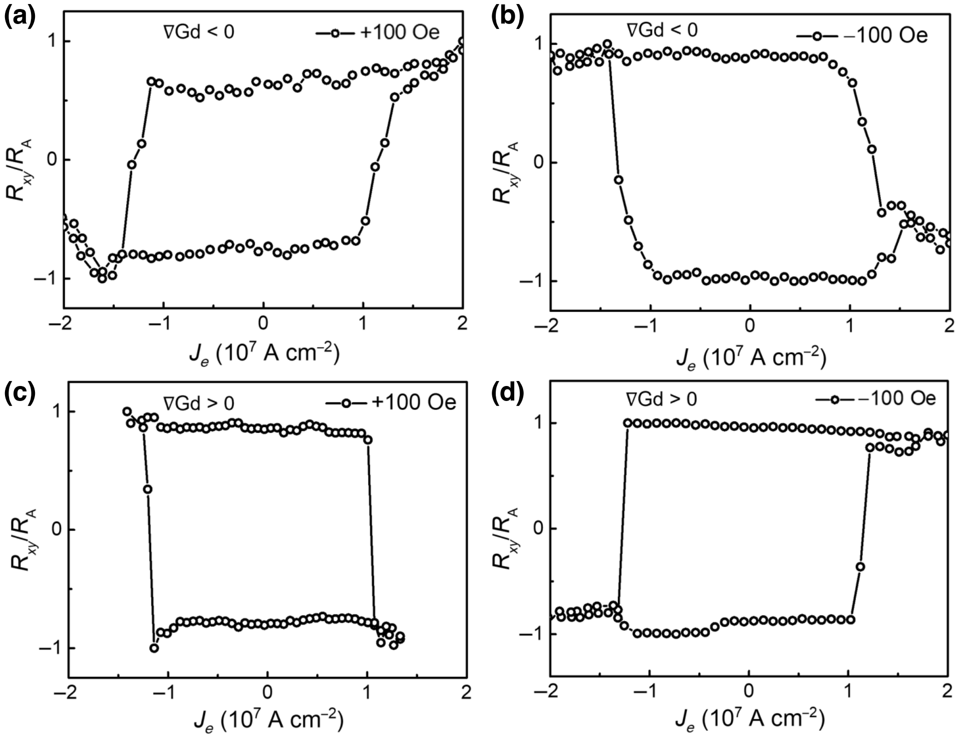

FIG. 3. (a),(b) Room-temperature current-induced SOT switching of the ∇Gd < 0 sample with an in-plane magnetic field H_x of ±100 Oe, respectively, and J_e is the current density in the Gd$_x$(FeCo)$_{1-x}$ layer. (c),(d) SOT switching of the ∇Gd > 0 sample with an in-plane magnetic field H_x of ±100 Oe, respectively.

field $H_{\mathrm{SOT}} = H_0 \sin\omega t$ generates the oscillation of the net magnetic moment around the x axis, which contributes to the second-harmonic Hall signal $R_{xy}^{2\omega}$. Since SOT can be divided into the fieldlike torque and the damping-like torque, the second-harmonic Hall resistance can be expressed as

$$R_{xy}^{2\omega} = \frac{R_{\mathrm{A}}}{2}\frac{H_{\mathrm{DL}}}{|H_x| - H_k} + R_P\frac{H_{\mathrm{FL}}}{|H_x|} + R_{\mathrm{ANE+SSE}}\frac{H_x}{|H_x|} + R_{\mathrm{offset}}, \tag{1}$$

where the first and second terms originate from the SOT-induced dampinglike (effective field H_{DL}) and fieldlike (effective field H_{FL}) torques, respectively. R_{A} and R_{P} represent the anomalous Hall and planar Hall resistance, respectively. $R_{\mathrm{ANE+SSE}}$ is the thermal contribution from anomalous Nernst and spin Seebeck effects, and R_{offset} is the signal offset. Figures 4(a) and 4(b) plot the first- and second-harmonic resistance $R_{xy}^{1\omega}$ and $R_{xy}^{2\omega}$ as a function of H_x of the ∇Gd < 0 sample. In Fig. 4(a), ∇Gd < 0 sample exhibits a strong perpendicular magnetic anisotropy, the H_k is determined to be 2.0 kOe. However, after the reversal of the compositional gradient, the perpendicular magnetic anisotropy of the film weakens with the $H_k = 1.0$ kOe, as shown in Fig. 4(c) for the ∇Gd > 0 sample. By fitting the $R_{xy}^{2\omega} - H_x$ curves [Fig. 4(b)] by Eq. (1), the effective field H_{DL} is obtained for −2.9 Oe at a current density of 2×10^6 A cm^{-2}. And H_{DL} is obtained for 3.1 Oe at a current density of 2×10^6 A cm^{-2} from Fig. 4(d). Then, the obtained SOT efficiency (H_{DL}/J_e) is -1.26×10^{-6} Oe A^{-1} cm^2 and 1.62×10^{-6} Oe A^{-1} cm^2 for the ∇Gd < 0 and ∇Gd > 0 samples, respectively, where H_{DL} is the SOT-induced out-of-plane effective field, as shown in Fig. 5. And the SOT efficiency value of two opposite gradient samples is very close. And the sign of that is opposite, due to the direction of the composition gradient.

Then, the current-induced hysteresis-loop shift method is employed to obtain the DMI field of the ∇Gd < 0 and ∇Gd > 0 samples. The bias field of the loop center with respect to the $H_z = 0$ is defined as H_z^{eff}, which can be considered as the effective field originating from the dampinglike torque. Figures 6(a) and 6(b) illustrate the $\chi_{\mathrm{SOT}} = H_z^{\mathrm{eff}}/j_e$ as a function of the in-plane magnetic field H_x for the ∇Gd < 0 and ∇Gd > 0 samples, respectively. Here, the χ_{SOT} first change quasilinearly with H_x and eventually saturate, which implies the effective field induced by the DMI (H_{DMI}). We estimated that the saturated value χ_{SOT} is about 1.62×10^{-6} Oe A^{-1} cm^2 and $|H_{\mathrm{DMI}}| \approx 49.9$ Oe for the ∇Gd < 0 sample in Fig. 6(a). For the ∇Gd > 0 sample [Fig. 6(b)], the saturated value χ_{SOT} is about 2.4×10^{-6} Oe A^{-1} cm^2 and $|H_{\mathrm{DMI}}| \approx 36.2$ Oe. Further, the magnitude of the DMI exchange constant D can be calculated from the measured $|H_{\mathrm{DMI}}|$ by using $D = \mu_0 M_s \delta_{\mathrm{DW}}$, where δ_{DW} is the DW width and relates to exchange stiffness constant A and effective PMA energy density K through $\delta_{\mathrm{DW}} = \pi\sqrt{\mathrm{A/K}}$. Using M_s by a superconducting quantum interface device (SQUID) at room temperature (see the Supplemental Material [44]), and assuming $A = 4 \times 10^{-12}$ J m^{-1} and $K = 2 \times 10^4$ J m^{-3} [49], we estimated $D = -28.7$ μJ m^{-2} for the ∇Gd < 0 sample, $D = 20.8$ μJ m^{-2} for the ∇Gd > 0 sample, respectively. Both the opposite-gradient samples show the opposite DMI and the magnitude of

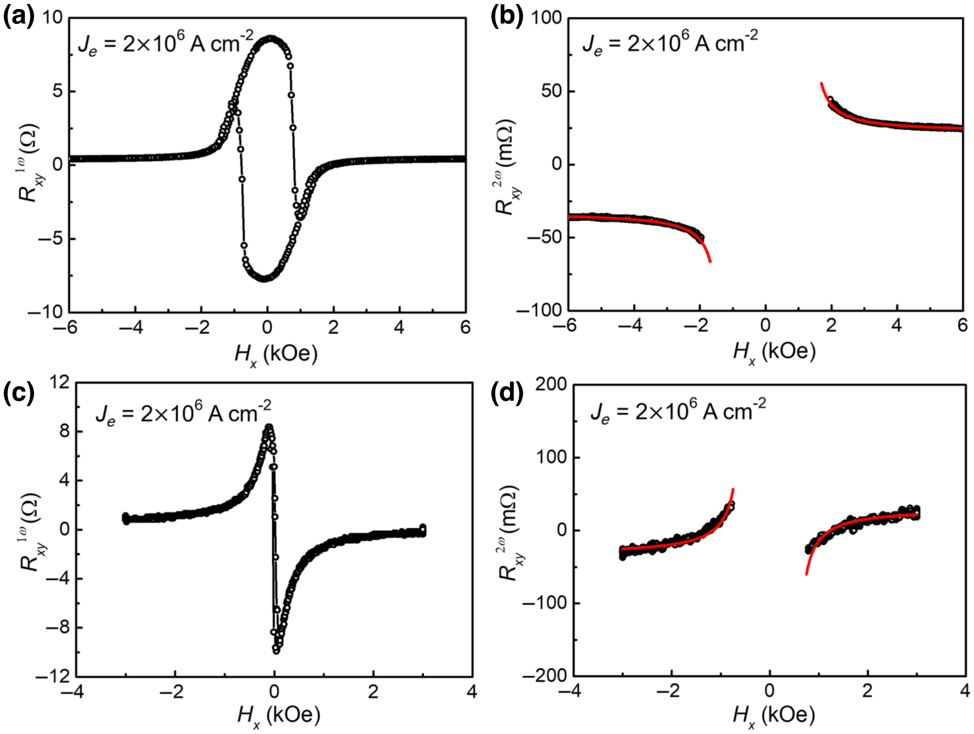

FIG. 4. Magnetic field along the x-direction dependence of (a) first- and (b) second-harmonic Hall resistances ($R_{xy}^{1\omega}$ and $R_{xy}^{2\omega}$) for the ∇Gd < 0 sample at a current density of 2×10^6 A cm^{-2}. (c),(d) $R_{xy}^{1\omega} - H_x$ and $R_{xy}^{2\omega} - H_x$ curves for the ∇Gd > 0 sample.

the DMI exchange constants are very close. Here, the obtained DMI, $\mathbf{D}_{\mathrm{IP}}$, is in-plane with the Néel type. Figures S6(a)–S6(d) in the Supplemental Material [44] show the represent magneto-optical Kerr effect (MOKE) images of the magnetic domain patterns by applying the magnetic field normal to the film (H_z) (see the Supplemental Material [44]). The best conditions to observe the isolated bubbles corresponding to the magnetic field are 180 and −160 Oe.

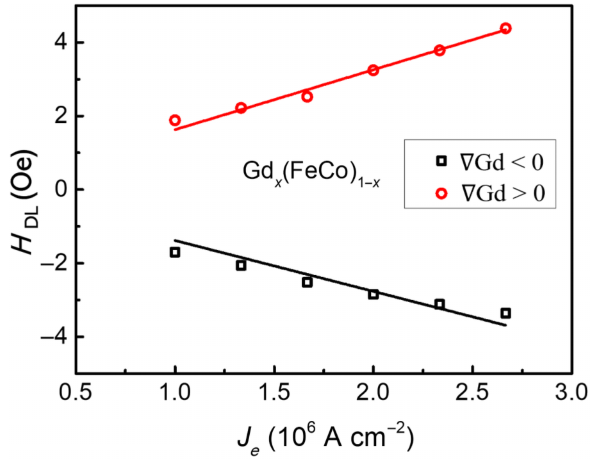

FIG. 5. Out-of-plane effective H_{DL} of SOT as a function of J_e for the ∇Gd < 0 (black hollow circles and ∇Gd > 0 (red hollow squares) samples, respectively. The corresponding slope obtained by linear fitting implies the effective SOT.

The combination of spin-orbit coupling and inversion symmetry breaking rise to the emergent phenomena: self-SOT and DMI. During the complex preparation process of Ta/Gd-Fe-Co layers with vertical composition gradient, the DMI-induced chiral symmetry breaking has been utilized to achieve the deterministic SOT switching in the previous work [50]. In the large family of magnetic rare-earth alloys and other 5d magnetic materials, spin torques and DMI in the symmetry-breaking single layer without the additional HM layer is of great interest. By precisely controlling the compositional gradient of Gd-Fe-Co films with the opposite composition gradient directions, the distributions of the noncolinear magnetic structures are observed in both cases. The DMI is induced with the combination of Bloch-type $\mathbf{D}_{\mathrm{OOP}}$ and Néel-type $\mathbf{D}_{\mathrm{IP}}$ in a single Gd-Fe-Co layer with a vertical composition gradient, which can destabilize the noncolinear magnetic structures. On one hand, consider two local magnetic atoms A and B at the same depth in Gd-Fe-Co (see schematic diagram in Fig. S7 in the Supplemental Material [44]), there is a mirror plane (m_{yz}) perpendicular to the line connecting the two atoms. Therefore, according to Moriya's rule [6], DMI between A and B ($\mathbf{D}_{AB}$) with Néel type is parallel to this m_{yz} plane. Since the in-plane component of the sample is still isotropic, thus the $\mathbf{D}_{\mathrm{OOP}}$ component of $\mathbf{D}_{AB}$ is not very large, that is, $\mathbf{D}_{AB}$ mainly contribute to the $\mathbf{D}_{\mathrm{IP}}$. On the other hand, for the magnetic atoms A and C at different depth in Gd-Fe-Co, a C_2 rotation axis cross the line connecting the two atoms. Therefore, the DMI between A and C ($\mathbf{D}_{AC}$) with Bloch type is parallel to this C_2 rotation axis,

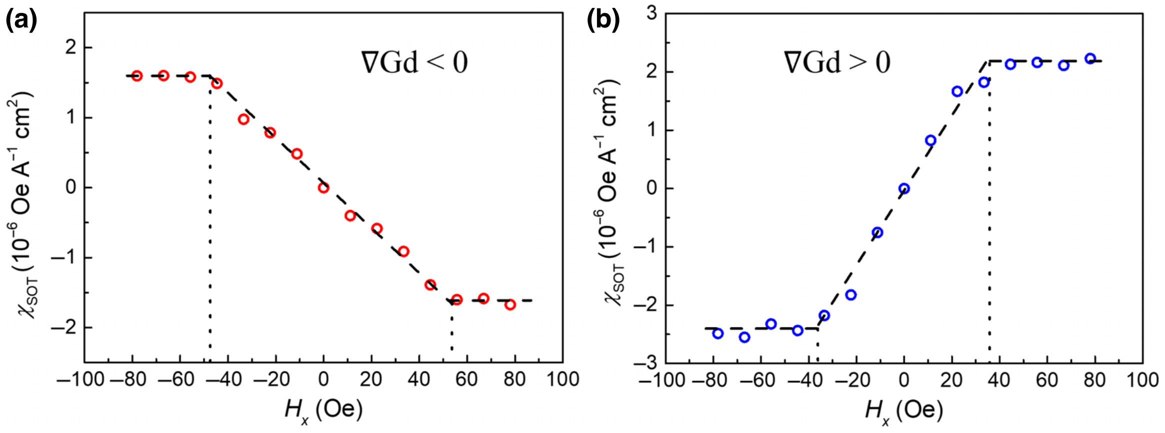

FIG. 6. (a),(b) The dependence of the effective SOT efficiency χ_{SOT} as a function of the magnetic field H_x for the ∇Gd < 0 and ∇Gd > 0 samples, respectively.

which results $\mathbf{D}_{AC}$ contribute to the $\mathbf{D}_{\text{OOP}}$. As a result, both $\mathbf{D}_{\text{IP}}$ and $\mathbf{D}_{\text{OOP}}$ present in the sample.

In addition, we realize the current-induced magnetization switching by self-SOT in the single magnetic layer with a composition gradient. Here, the self-SOT and the noncolinear magnetic phase are not directly related to each other, even though both the self-SOT and the noncolinear magnetic phase originates from the composition gradient-induced inversion symmetry breaking. Also, when we reverse the composition gradient of $\text{Gd}_x(\text{FeCo})_{1-x}$, both signs of SOT and $\mathbf{D}_{\text{IP}}$ change, this indicates the symmetry-breaking-related effects in our system. Zhang *et al.* [51] also reported the significance of spatial magnetic distributions, which strongly affect the dynamic response of the ferrimagnet order by using a two-dimensional atomistic model. The work presented in this study can provide a better understanding of the ferrimagnetic behavior with the nonuniform magnetic distribution.

There are other possibilities for the helical state we observed, such as the chiral *xy* model in the frustrated magnetic system, which typically happens at low temperatures; in our work, the conical states are observed at room temperature where the $k_{\text{B}}\text{T}$ energy will strongly disturb the frustrated states; and also the Gd-Fe-Co in our work is the amorphous structure not the crystal structure, therefore, we think the chiral *xy* model does not apply in our system.

III. CONCLUSION

In conclusion, we report the conical magnetic structure, the bulk SOT and the combination of Bloch- and Néel-type DMI induced in a single Gd-Fe-Co layer with a vertical composition gradient. The PNR results provide the detailed depth-dependent magnetic structure of films at different magnetic fields and observe the oscillation in **M** with a noncollinear structure, suggesting the nonzero out-of-plane Bloch-type $\mathbf{D}_{\text{OOP}}$. We utilize the bulk SOT induced by the composition gradient to realize the SOT switching of the magnetization, and the in-plane Néel-type $\mathbf{D}_{\text{IP}}$ is also obtained from the saturation field of the χ_{SOT}. With tuning the composition gradient along the opposite direction, the SOT and $\mathbf{D}_{\text{IP}}$ are shown in opposite signs and the magnitude constants are close to each other. This work provides an insight into understanding the magnetic order in the FMI single layer and may advance the practical applications exploiting the rich physics of spin-orbit effects. We note that large tunnel magnetoresistance (TMR) ratios have been demonstrated in magnetic tunnel junctions based on FIMs [52–54]. Therefore, the Gd-Fe-Co gradient thin film proposed in this paper can be integrated with MTJ structures for future SOT-based magnetic random-access memory applications without additional SOC layers.

ACKNOWLEDGMENTS

This work was partially supported by the National Key Research and Development Program of China (Grant No. 2022YFA1402801), the National Natural Science Foundation of China (NSFC, Grants No. 52271239, No. 12134017, No. 12304149), the Guangdong Basic and Applied Basic Research Foundation (Grant Nos. 2022B1515120058, No. 2022A1515110648, No. 2023A1515010953), and the start-up funding from Songshan Lake Materials Laboratory (Grant No. Y1D1071S511). The work at UCLA was supported by the U.S. Army Research Office MURI program under Grants No. W911NF-16-1-0472 and No. W911NF-20-2-0166. This research used resources at the Spallation Neutron Source, a DOE Office of Science User Facility operated by the Oak Ridge National Laboratory.

[1] F. Katmis, V. Lauter, F. S. Nogueira, B. A. Assaf, M. E. Jamer, P. Wei, B. Satpati, J. W. Freeland, I. Eremin,

D. Heiman, P. Jarillo-Herrero, and J. S. Moodera, A high-temperature ferromagnetic topological insulating phase by proximity coupling, Nature **533**, 513 (2016).

[2] A. Büse, M. L. Juan, N. Tischler, V. D'Ambrosio, F. Sciarrino, L. Marrucci, and G. Molina-Terriza, Symmetry protection of photonic entanglement in the interaction with a single nanoaperture, Phys. Rev. Lett. **121**, 173901 (2018).

[3] D. V. Else, I. Schwarz, S. D. Bartlett, and A. C. Doherty, Symmetry-protected phases for measurement-based quantum computation, Phys. Rev. Lett. **108**, 240505 (2012).

[4] E. Khalaf, Higher-order topological insulators and superconductors protected by inversion symmetry, Phys. Rev. B **97**, 205136 (2018).

[5] S. Sumita and Y. Yanase, Unconventional superconducting gap structure protected by space group symmetry, Phys. Rev. B **97**, 134512 (2018).

[6] T. Moriya, Anisotropic superexchange interaction and weak ferromagnetism, Phys. Rev. **120**, 91 (1960).

[7] I. Dzyaloshinsky, A thermodynamic theory of "weak" ferromagnetism of antiferromagnetics, J. Phys. Chem. Solids **4**, 241 (1957).

[8] F. Jonietz, S. Mühlbauer, C. Pfleiderer, A. Neubauer, W. Münzer, A. Bauer, T. Adams, R. Georgii, P. Böni, R. A. Duine, K. Everschor, M. Garst, and A. Rosch, Spin transfer torques in MnSi at ultralow current densities, Science **330**, 1648 (2010).

[9] A. Fert, V. Cros, and J. Sampaio, Skyrmions on the track, Nat. Nanotechnol. **8**, 152 (2013).

[10] J. Sampaio, V. Cros, S. Rohart, A. Thiaville, and A. Fert, Nucleation, stability and current-induced motion of isolated magnetic skyrmions in nanostructures, Nat. Nanotechnol. **8**, 839 (2013).

[11] S. Emori, U. Bauer, S.-M. Ahn, E. Martinez, and G. S. D. Beach, Current-driven dynamics of chiral ferromagnetic domain walls, Nat. Mater. **12**, 611 (2013).

[12] K. S. Ryu, L. Thomas, S. H. Yang, and S. Parkin, Chiral spin torque at magnetic domain walls, Nat. Nanotechnol. **8**, 527 (2013).

[13] O. Boulle, S. Rohart, L. D. Buda-Prejbeanu, E. Jue, I. M. Miron, S. Pizzini, J. Vogel, G. Gaudin, and A. Thiaville, Domain wall tilting in the presence of the Dzyaloshinskii-Moriya interaction in out-of-plane magnetized magnetic nanotracks, Phys. Rev. Lett. **111**, 217203 (2013).

[14] G. Chen, J. Zhu, A. Quesada, J. Li, A. T. N'Diaye, Y. Huo, T. P. Ma, Y. Chen, H. Y. Kwon, C. Won, Z. Q. Qiu, A. K. Schmid, and Y. Z. Wu, Novel chiral magnetic domain wall structure in Fe/Ni/Cu(001) films, Phys. Rev. Lett. **110**, 177204 (2013).

[15] A. Fert, N. Reyren, and V. Cros, Magnetic skyrmions: Advances in physics and potential applications, Nat. Rev. Mater. **2**, 17031 (2017).

[16] Wanjun Jiang, Pramey Upadhyaya, Wei Zhang, Guoqiang Yu, M. Benjamin Jungfleisch, Frank Y. Fradin, John E. Pearson, Yaroslav Tserkovnyak, Kang L. Wang, Olle Heinonen, Suzanne G. E. te Velthuis, and A. Hoffmann, Blowing magnetic skyrmion bubbles, Science **349**, 283 (2015).

[17] S. Woo, K. Litzius, B. Kruger, M. Y. Im, L. Caretta, K. Richter, M. Mann, A. Krone, R. M. Reeve, M. Weigand, P. Agrawal, I. Lemesh, M. A. Mawass, P. Fischer, M. Klaui, and G. S. Beach, Observation of room-temperature magnetic skyrmions and their current-driven dynamics in ultrathin metallic ferromagnets, Nat. Mater. **15**, 501 (2016).

[18] Z. C. Luo, T. P. Dao, A. Hrabec, J. Vijayakumar, A. Kleibert, M. Baumgartner, E. Kirk, J. Z. Cui, T. Savchenko, G. Krishnaswamy, L. J. Heyderman, and P. Gambardella, Chirally coupled nanomagnets, Science **363**, 1435 (2019).

[19] A. Manchon, J. Železný, I. M. Miron, T. Jungwirth, J. Sinova, A. Thiaville, K. Garello, and P. Gambardella, Current-induced spin-orbit torques in ferromagnetic and antiferromagnetic systems, Rev. Mod. Phys. **91**, 035004 (2019).

[20] M. I. Dyakonov and V. I. Perel, Current-induced spin orientation of electrons in semiconductors, Phys. Rev. A **35**, 459 (1971).

[21] J. Sinova, S. O. Valenzuela, J. Wunderlich, C. H. Back, T. Jungwirth, and Spin Hall effects. Rev. Mod. Phys. **87**, 1213 (2015).

[22] L. Q. Liu, C. F. Pai, Y. Li, H. W. Tseng, D. C. Ralph, and R. A. Buhrman, Spin-torque switching with the giant spin Hall effect of tantalum, Science **336**, 555 (2012).

[23] Y. A. Bychkov and E. I. Rashba, Oscillatory effects and the magnetic susceptibility of carriers in inversion layers, J. Phys. C: Solid State Phys. **17**, 6039 (1984).

[24] A. Manchon and S. Zhang, Theory of spin torque due to spin-orbit coupling, Phys. Rev. B **79**, 094422 (2009).

[25] I. M. Miron, K. Garello, G. Gaudin, P. J. Zermatten, M. V. Costache, S. Auffret, S. Bandiera, B. Rodmacq, A. Schuhl, and P. Gambardella, Perpendicular switching of a single ferromagnetic layer induced by in-plane current injection, Nature (London) **476**, 189 (2011).

[26] K. Y. R. Yoshimi, A. Tsukazaki, K. S. Takahashi, M. Kawasaki, and Y. Tokura, Current-driven magnetization switching in ferromagnetic bulk Rashba semiconductor (Ge, Mn)Te, Sci. Adv. **4**, eaat9989 (2018).

[27] S. Y. Bodnar, L. Smejkal, I. Turek, T. Jungwirth, O. Gomonay, J. Sinova, A. A. Sapozhnik, H. J. Elmers, M. Klaui, and M. Jourdan, Writing and reading antiferromagnetic Mn_2Au by Neel spin-orbit torques and large anisotropic magnetoresistance, Nat. Commun. **9**, 348 (2018).

[28] R. Mishra, J. Yu, X. Qiu, M. Motapothula, T. Venkatesan, and H. Yang, Anomalous current-induced spin torques in ferrimagnets near compensation, Phys. Rev. Lett. **118**, 167201 (2017).

[29] R. Bläsing, T. Ma, S.-H. Yang, C. Garg, F. K. Dejene, A. T. N'Diaye, G. Chen, K. Liu, and S. S. P. Parkin, Exchange coupling torque in ferrimagnetic Co/Gd bilayer maximized near angular momentum compensation temperature, Nat. Commun. **9**, 4984 (2018).

[30] T. Okuno, D.-H. Kim, S.-H. Oh, S. K. Kim, Y. Hirata, T. Nishimura, W. S. Ham, Y. Futakawa, H. Yoshikawa, A. Tsukamoto, Y. Tserkovnyak, Y. Shiota, T. Moriyama, K.-J. Kim, K.-J. Lee, and T. Ono, Spin-transfer torques for domain wall motion in antiferromagnetically coupled ferrimagnets, Nat. Electron. **2**, 389 (2019).

[31] Y. Hirata, D.-H. Kim, S. K. Kim, D.-K. Lee, S.-H. Oh, D.-Y. Kim, T. Nishimura, T. Okuno, Y. Futakawa, H. Yoshikawa, A. Tsukamoto, Y. Tserkovnyak, Y. Shiota, T. Moriyama, S.-B. Choe, K.-J. Lee, and T. Ono, Vanishing

skyrmion Hall effect at the angular momentum compensation temperature of a ferrimagnet, Nat. Nanotechnol. **14,** 232 (2019).

[32] S. Woo, K. M. Song, X. Zhang, Y. Zhou, M. Ezawa, X. Liu, S. Finizio, J. Raabe, N. J. Lee, S.-I. Kim, S.-Y. Park, Y. Kim, J.-Y. Kim, D. Lee, O. Lee, J. W. Choi, B.-C. Min, H. C. Koo, and J. Chang, Current-driven dynamics and inhibition of the skyrmion Hall effect of ferrimagnetic skyrmions in GdFeCo films, Nat. Commun. **9**, 959 (2018).

[33] Z. Zheng, Y. Zhang, V. Lopez-Dominguez, L. Sanchez-Tejerina, J. Shi, X. Feng, L. Chen, Z. Wang, Z. Zhang, K. Zhang, B. Hong, Y. Xu, Y. Zhang, M. Carpentieri, A. Fert, G. Finocchio, W. Zhao, and P. Khalili Amiri, Field-free spin-orbit torque-induced switching of perpendicular magnetization in a ferrimagnetic layer with a vertical composition gradient, Nat. Commun. **12**, 4555 (2021).

[34] Q. Zhang, J. Liang, K. Bi, L. Zhao, H. Bai, Q. Cui, H. A. Zhou, H. Bai, H. Feng, W. Song, G. Chai, O. Gladii, H. Schultheiss, T. Zhu, J. Zhang, Y. Peng, H. Yang, and W. Jiang, Quantifying the Dzyaloshinskii-Moriya interaction induced by the bulk magnetic asymmetry, Phys. Rev. Lett. **128**, 167202 (2022).

[35] O. Krupin, G. Bihlmayer, K. Starke, S. Gorovikov, J. E. Prieto, K. Döbrich, S. Blügel, and G. Kaindl, Rashba effect at magnetic metal surfaces, Phys. Rev. B **71**, 201403(R) (2005).

[36] D. Céspedes-Berrocal, H. Damas, S. Petit-Watelot, D. Maccariello, P. Tang, A. Arriola-Córdova, P. Vallobra, Y. Xu, J. L. Bello, E. Martin, S. Migot, J. Ghanbaja, S. Zhang, M. Hehn, S. Mangin, C. Panagopoulos, V. Cros, A. Fert, and J. C. Rojas-Sánchez, Current-induced spin torques on single GdFeCo magnetic layers, Adv. Mater. **33**, 2007047 (2021).

[37] I. A. Nechaev and E. E. Krasovskii, Relativistic splitting of surface states at Si-terminated surfaces of the layered intermetallic compounds RT_2Si_2(R = rare earth; T = Ir, Rh), Phys. Rev. B **98**, 245415 (2018).

[38] D. Y. Usachov, *et al.*, Cubic Rashba effect in the surface spin structure of rare-earth ternary materials, Phys. Rev. Lett. **124**, 237202 (2020).

[39] H. Wu, Y. Xu, P. Deng, Q. Pan, S. A. Razavi, K. Wong, L. Huang, B. Dai, Q. Shao, G. Yu, X. Han, J. C. Rojas-Sánchez, S. Mangin, and K. L. Wang, Spin-orbit torque switching of a nearly compensated ferrimagnet by topological surface states, Adv. Mater. **31**, 1901681 (2019).

[40] V. Lauter, H. Ambaye, R. Goyette, W.-T. Hal Lee, and A. Parizzi, Highlights from the magnetism reflectometer at the SNS, Phys. B **404**, 2543 (2009).

[41] M. R. Fitzsimmons and T. R. Charlton, Tools to perform data reduction of time-of-flight data taken on BL4A (MagRef)—a Jupyter notebook approach (2020). https://doi.org/10.5281/zenodo.3968838

[42] M. R. Fitzsimmons, Code to Qz-bin polarized neutron reflectivity data accounting for Zeeman energy splitting of spin-flip reflection, (2020). https://zenodo.org/record/3828984#.XyMIQUl7lZohttps://doi.org/10.5281/zenodo.3828984

[43] T. R. Charlton and M. R. Fitzsimmons, Fitzsimmons, Code to obtain single event data from Spallation Neutron Source Beamline-4A (MagRef) (2020). https://zenodo.org/record/3967680#.XyMUDUl7nBUhttps://doi.org/10.5281/zenodo.3967680

[44] See Supplemental Material at http://link.aps.org/supplemental/10.1103/PhysRevApplied.21.014045 for PNR measurements, magnetic properties, and MOKE images.

[45] J. D. Hoffman, B. J. Kirby, J. Kwon, G. Fabbris, D. Meyers, J. W. Freeland, I. Martin, O. G. Heinonen, P. Steadman, H. Zhou, C. M. Schlepütz, M. P. M. Dean, S. G. E. te Velthuis, J.-M. Zuo, and A. Bhattacharya, Oscillatory noncollinear magnetism induced by interfacial charge transfer in superlattices composed of metallic oxides, Phys. Rev. X **6**, 041038 (2016).

[46] J. F. Lynn and P. A. Seeger, Resonance effecs in neutron scattering of rare-earth nuclides, At. Data Nucl. Data Tables **44**, 191 (1990).

[47] Q. Shao, G. Yu, Y.-W. Lan, Y. Shi, M.-Y. Li, C. Zheng, X. Zhu, L.-J. Li, P. K. Amiri, and K. L. Wang, Strong Rashba-Edelstein effect-induced spin–orbit torques in monolayer transition metal dichalcogenide/ferromagnet bilayers, Nano Lett. **16**, 7514 (2016).

[48] M. Hayashi, J. Kim, M. Yamanouchi, and H. Ohno, Quantitative characterization of the spin-orbit torque using harmonic Hall voltage measurements, Phys. Rev. B **89**, 144425 (2014).

[49] L. Caretta, M. Mann, F. Büttner, K. Ueda, B. Pfau, C. M. Günther, P. Hessing, A. Churikova, C. Klose, M. Schneider, D. Engel, C. Marcus, D. Bono, K. Bagschik, S. Eisebitt, and G. S. D. Beach, Fast current-driven domain walls and small skyrmions in a compensated ferrimagnet, Nat. Nanotechnol. **13**, 1154 (2018).

[50] H. Wu, J. Nance, S. A. Razavi, D. Lujan, B. Dai, Y. Liu, H. He, B. Cui, D. Wu, K. Wong, K. Sobotkiewich, X. Li, G. P. Carman, and K. L. Wang, Chiral symmetry breaking for deterministic switching of perpendicular magnetization by spin–orbit torque, Nano Lett. **21**, 515 (2020).

[51] X. Zhang, B. Cai, J. Ren, Z. Yuan, Z. Xu, Y. Yang, G. Liang, and Z. Zhu, Spatially nonuniform oscillations in ferrimagnets based on an atomistic model, Phys. Rev. B **106**, 184419 (2022).

[52] X. J. Bai, J. Du, J. Zhang, B. You, L. Sun, W. Zhang, A. Hu, and S. M. Zhou, Influence of the thickness of the FeCoGd layer on the magnetoresistance in FeCoGd-based spin valves and magnetic tunnel junctions, J. Phys. D: Appl. Phys. **41**, 215008 (2008).

[53] J. Jeong, Y. Ferrant, S. V. Faleev, M. G. Samant, C. Felser, and S. S. P. Parkin, Termination layer compensated tunnelling magnetoresistance in ferrimagnetic Heusler compounds with high perpendicular magnetic anisotropy, Nat. Commun. **7**, 10276 (2016).

[54] A. K. Reza and K. Roy, Fast switching in CoTb based ferrimagnetic tunnel junction, J. Appl. Phys. **126**, 023901 (2019).

Correction: The name of the tenth author contained an error and has been fixed.